

# JGR Space Physics

## RESEARCH ARTICLE

10.1029/2021JA029205

### Key Points:

- Statistical patterns of the total downward Poynting flux into the atmosphere have been derived using Super Dual Auroral Radar Network and Active Magnetosphere and Planetary Electrodynamics Response Experiment data
- Statistical patterns of neutral mass density perturbations as a percentage of the background density have been derived using Challenging Minisatellite Payload data
- Mesoscale downward Poynting flux in the cusp region do not correlate very well with neutral mass density enhancements at a similar scale

### Correspondence to:

D. D. Billett,  
[daniel.billett@usask.ca](mailto:daniel.billett@usask.ca)

### Citation:








Billett, D. D., Perry, G. W., Clausen, L. B. N., Archer, W. E., McWilliams, K. A., Haaland, S., et al. (2021). The relationship between large scale thermospheric density enhancements and the spatial distribution of Poynting flux. *Journal of Geophysical Research: Space Physics*, 126, e2021JA029205. <https://doi.org/10.1029/2021JA029205>

Received 3 FEB 2021  
Accepted 18 APR 2021

© 2021. The Authors.

This is an open access article under the terms of the [Creative Commons Attribution-NonCommercial License](https://creativecommons.org/licenses/by-nc/4.0/), which permits use, distribution and reproduction in any medium, provided the original work is properly cited and is not used for commercial purposes.

# The Relationship Between Large Scale Thermospheric Density Enhancements and the Spatial Distribution of Poynting Flux

D. D. Billett<sup>1</sup> , G. W. Perry<sup>2</sup> , L. B. N. Clausen<sup>3</sup> , W. E. Archer<sup>1</sup> , K. A. McWilliams<sup>1</sup> , S. Haaland<sup>4,8,9</sup> , J. P. Reistad<sup>4</sup> , J. K. Burchill<sup>5</sup> , M. R. Patrick<sup>5</sup>, B. K. Humberst<sup>6</sup> , and B. J. Anderson<sup>7</sup> 

<sup>1</sup>Institute of Space and Atmospheric Studies, University of Saskatchewan, Saskatoon, SK, Canada, <sup>2</sup>Center for Solar-Terrestrial Research, New Jersey Institute of Technology, Newark, NJ, USA, <sup>3</sup>Department of Physics, University of Oslo, Oslo, Norway, <sup>4</sup>Birkeland Centre for Space Science, Department of Physics and Technology, University of Bergen, Bergen, Norway, <sup>5</sup>Department of Physics and Astronomy, University of Calgary, Calgary, AB, Canada, <sup>6</sup>Faculty of Humanities and Education, Volda University College, Volda, Norway, <sup>7</sup>Applied Physics Laboratory, Johns Hopkins University, Laurel, MD, USA, <sup>8</sup>Max-Planck-Institut für Sonnensystemforschung, Göttingen, Germany, <sup>9</sup>The University Centre in Svalbard, Longyearbyen, Svalbard

**Abstract** Large thermospheric neutral density enhancements in the cusp region have been examined for many years. The Challenging Minisatellite Payload (CHAMP) satellite for example has enabled many observations of the perturbation, showing that it is mesoscale in size and exists statistically over solar cycle timescales. Further studies examining the relationship with magnetospheric energy input have shown that fine-scale Poynting fluxes are associated with the density perturbations on a case-by-case basis, whilst others have found that mesoscale downward fluxes also exist in the cusp region statistically. In this study, we use nearly 8 years of the overlapping Super Dual Auroral Radar Network and Active Magnetosphere and Planetary Electrodynamics Response Experiment datasets to generate global-scale patterns of the high-latitude and height-integrated Poynting flux into the ionosphere, with a time resolution of 2 min. From these, average patterns are generated based on the interplanetary magnetic field orientation. We show the cusp is indeed an important feature in the Poynting flux maps, but the magnitude does not correlate well with statistical neutral mass density perturbations observed by the CHAMP satellite on similar spatial scales. Importantly, the lack of correlation between mesoscale height-integrated Poynting fluxes and the cusp neutral mass density enhancement gives possible insight into other processes that may account for the discrepancy, such as energy deposition at finer scale sizes or at higher altitudes than captured.

## 1. Introduction

The density of the neutral thermosphere at high latitudes is primarily modulated by changes in solar irradiance, and by magnetospheric interactions with the solar wind causing energy to be transported down magnetic field lines (Pröls, 2011). The former is regular and predictable, which controls the “background” neutral density, whilst the latter can be considered as a cause of perturbations above the background.

The cusp enhancement is a well-known neutral density perturbation in the high-latitude thermosphere. The first observations were by Lühr et al. (2004), who found significantly enhanced neutral densities in the dayside cusp region (~68–75° geomagnetic latitude, 10–12 magnetic local time [MLT]) during several passes of the Challenging Minisatellite Payload (CHAMP; Reigber et al., 2002) at around 400 km altitude. It was subsequently shown by H. Liu et al. (2005) and Schlegel et al. (2005) that the cusp enhancement existed even under average conditions and during geomagnetically quiet times, with a 20%–30% increase above the background neutral density (i.e., that caused by irradiance), that was not able to be predicted by global circulation models of the neutral winds and densities. These studies ultimately confirmed what had been strongly suspected for a few decades, that solar wind energy was directly influencing the high-latitude upper thermospheric structure. A review of this history up to the early CHAMP observations can be found in Moe and Moe (2008). The mechanism by which the cusp density enhancement is generated is still not well understood.

A survey of density enhancements seen by CHAMP during geomagnetic storms by R. Liu et al. (2010) found that they are typically less than 900 km in latitudinal width, and occur during all interplanetary magnetic field (IMF) orientations (although greater magnitudes of perturbation tend to occur during negative IMF  $B_z$  conditions; Rentz & Lühr, 2008). Lühr et al. (2004) originally attributed the cusp enhancement to intense small scale ( $\sim 10$ s of km) field-aligned currents (FACs) and their associated electric fields, which would drive Joule heating and upwelling of the neutral gas. However, the aforementioned R. Liu et al. (2010) survey found that only around half of events coincided with strong FACs. Simulations by Demars and Schunk (2007) showed that cusp ion heating events would indeed generate a thermospheric upwelling, but only when increasing the ion-neutral frictional heating term by a factor of 110 to simulate extreme events.

In contrast, Clemmons et al. (2008) found a density depletion of a few percent about 150 km below the CHAMP orbital altitude within the dayside cusp vicinity, utilizing complementary neutral density data from the Streak mission (Clemmons et al., 2009). The depletion was thought to be indicative of the short penetration depth of soft particle precipitation in the cusp region, and upon modeling, was found to have produced the thermospheric upwelling theorized by previous studies at 400 km altitude (e.g., Demars & Schunk, 2007), but not in the upper E-region. Subsequently, Deng et al. (2011) decoupled the effects of Joule heating deposited at both low ( $< 150$  km) and high ( $> 300$  km) altitudes, showing that much of the temporal variation of the atmospheric upwelling at CHAMP altitudes ( $\sim 350$ – $450$  km) was caused by low altitude heating, but F-region Joule heating was primarily responsible for the neutral density and vertical wind enhancements. This importance of F-region heating was attributed to the higher heating per unit mass in the F region compared to the E region, and indicated that E-region Joule heating associated with FAC closure could not be fully responsible for density enhancements seen in the F-region. Brinkman et al. (2016) later found, in agreement with the conclusions by Clemmons et al. (2009) and Deng et al. (2011), that the low altitude density depletion was probably due to the neutral gas being transported upwards as the thermosphere expands. Brinkman et al. (2016) also saw soft particle precipitation heating playing an important role in driving a cusp neutral density enhancement.

Crowley et al. (2010) was able to reproduce a cusp enhancement observed by CHAMP using the Assimilative mapping of ionospheric electrodynamics (AMIE; Richmond, 1992) as input to the TIME-GCM (Roble & Ridley, 1994) during an extreme geomagnetic storm. A DMSP satellite, that was included in the assimilation, saw large and localized downward Poynting fluxes in the cusp region during the event. Indeed, Knipp et al. (2011) showed statistically that very large magnitudes of Poynting flux into the cusp were common during events where the IMF magnitude was  $> 10$  nT. Deng et al. (2013), utilizing the Global Ionosphere-Thermosphere Model (GITM; Ridley et al., 2006), also found that a very large magnitude of Poynting flux imposed on the ionosphere generated a cusp density enhancement by as much as 29% in the F region due to soft particle precipitation and Joule heating. These studies however did not explain the existence of the cusp neutral density enhancement during geomagnetically quiet times. It should also be noted that the total magnitude of Poynting flux when it is dissipated in the ionosphere is split between Joule heating and mechanical work, with Joule heating being dominant most of the time (Thayer et al., 1995). Joule heating, as it is dependent on the Pedersen conductivity, is highest in the E-region, but still has significant effects on the F-region thermosphere due to the low neutral density (Billett et al., 2020), and during cases such as that described by Deng et al. (2013) mentioned previously.

In the empirical model of Poynting flux developed by Cosgrove et al. (2014), the cusp was highlighted as a region of strong downward Poynting flux under northward IMF conditions. This was in stark contrast to previous empirical models, such as that by Weimer (2005), which showed no significant amount of energy in the cusp region under any IMF orientation. This difference was attributed to the use of a separate empirical electric field model in the older studies that would not have captured the variability of the field well, which is a known shortcoming that results in underestimating the total energy dissipation into the ionosphere (e.g., Codrescu et al., 1995). Electric field variability in the cusp region can indeed be high, but the IMF orientation may not be a good descriptor of that variability (Cosgrove & Thayer, 2006; Förster et al., 2007). In the statistical study of Joule heating by Billett et al. (2018), cusp enhancements were seen to have both a universal time and seasonal dependence, which is more indicative of variations in the dayside conductivity than electric field variability.

In this study, we develop statistical high latitude Poynting flux distributions and compare them to statistical distributions of neutral mass density enhancements. We employ  $\sim 10$  years of neutral density measurements from the CHAMP satellite (Doornbos et al., 2010; Reigber et al., 2002), along with global scale calculations of Poynting flux using  $\sim 7$  years of data from the Active Magnetosphere and Planetary Electrodynamics Response Experiment (AMPERE; Anderson et al., 2014) and the Super Dual Auroral Radar Network (SuperDARN; Greenwald et al., 1995). Our statistical Poynting flux patterns based on IMF orientation are the first to be created using the combined AMPERE and SuperDARN datasets, whilst neutral density perturbations within the well-established CHAMP data set are found using a novel technique which highlights the cusp in relation to the surrounding areas. It is shown that whilst our patterns of Poynting flux and neutral mass density perturbations are consistent with many previous studies, there does not appear to be a strong correlation between them in terms of both morphology and magnitude on mesoscales. This implies that at least one underlying process, whether because it is happening at a smaller scale or otherwise, is not being captured by our analysis.

## 2. Data

### 2.1. Neutral Density Perturbation

The CHAMP satellite was launched in 2000 into a nearly circular orbit which gradually decreased from an altitude of approximately 450 km until it re-entered the Earth's atmosphere in 2010. The accelerometer on board CHAMP enabled the detection of neutral mass density perturbations as small as  $1 \times 10^{-14} \text{ kg m}^{-3}$ , with a time resolution of 10 s. The full pre-processed data set of neutral densities over the entire lifetime of CHAMP, including positional information, can be obtained from Förster and Doornbos (2019). Due to the variations in altitude, previous studies utilizing CHAMP measurements have typically normalized neutral densities to a common altitude using models for the thermospheric scale height (e.g., H. Liu et al., 2005). We have instead derived neutral mass density perturbations from a running average “background” density, that is, a deviation from the density which is driven by Solar Extreme Ultraviolet (EUV) flux, similar to the method employed by Clausen et al. (2014) and Clemmons et al. (2008).

For a neutral mass density point measurement made by CHAMP ( $\rho$ ), a background neutral mass density ( $\langle \rho \rangle$ ), which is made up of an average of the previous 5 min of measured densities, is subtracted. This background density spans approximately  $20^\circ$  of magnetic latitude along the CHAMP orbital track, or 30 measurements. The calculated value is then normalized as a fraction of the background neutral mass density, giving a perturbation mass density ( $\Delta\rho$ ) that is in terms of fractional percent:

$$\Delta\rho = \frac{\rho - \langle \rho \rangle}{\langle \rho \rangle} \quad (1)$$

$\Delta\rho$  will hold both temporal and spatial perturbations, but the timescale upon which the thermospheric density changes is almost certainly several hours longer than the 5 min captures by the background density average, for all altitudes seen by CHAMP (Sutton et al., 2009; Wang et al., 2020; Wilson et al., 2006). Therefore,  $\Delta\rho$  is almost entirely a measure of how the region of interest compares to the region the satellite has just passed through. A 5-min timescale for  $\langle \rho \rangle$  is short enough that large scale features, such as density enhancements due to changing solar irradiance with proximity to the sub-solar point, should be mostly removed from  $\Delta\rho$ .

As the CHAMP data set spans many years, encompassing both the peak of solar cycle 23 and a portion of the cycle 24 incline, it is important that the significant effects of solar EUV on the neutral mass density (Walterscheid, 1989) is minimized in our results. Using this method for determining a perturbation neutral mass density, rather than looking at altitude-normalized densities, almost entirely removes the effect of changing solar flux (e.g., the  $f_{10.7}$  radio emission) due to only sampling the past 5 min of data for each data point. Additionally, the short timescale used also minimizes seasonal and altitude density variations. This process does very well at extracting only density changes that are due to spatial inhomogeneities, but is subsequently unable to show temporal changes in a particular region due to events such as substorms unless the density change happens unprecedentedly fast. Substorms are unlikely to have a significant effect on cusp neutral densities however, as they are primarily a nightside phenomenon. The technique for extracting





## 2.2. Poynting Flux

The perturbation Poynting vector  $\mathbf{S}_{\parallel}$ , that is, the total amount of energy dissipated in the ionosphere via FACs, is given by Waters et al. (2004):

$$\mathbf{S}_{\parallel} = -\frac{1}{\mu_0}(\mathbf{E} \times \delta\mathbf{B}) \cdot \hat{\mathbf{r}} \quad (2)$$

where  $\mu_0$  is the permeability of free space,  $\mathbf{E}$  is the ionospheric electric field,  $\delta\mathbf{B}$  is the perturbation magnetic field (deviation from the terrestrial field) and  $\hat{\mathbf{r}}$  is the unit vector parallel to the geomagnetic field.  $\mathbf{S}_{\parallel}$  is positive downward, indicating the magnetosphere is driving the ionosphere. Negative (or upward) Poynting flux indicates that the ionosphere might be driving the magnetosphere as a current generator through the ionospheric wind dynamo. We obtain electric field information from the SuperDARN and perturbation magnetic field measurements from AMPERE, both on a global scale, combining them using Equation 2 and the method described by Waters et al. (2004) onto the same grid used for neutral density perturbations.

Overlapping AMPERE and SuperDARN data currently exists between years, 2010 and 2017, and like the neutral density binning process, we have also not filtered the times for steady IMF conditions. It is important to note that by not filtering the AMPERE and SuperDARN datasets in this way, we do not account for the fact that the ionosphere does not immediately and fully respond to a change in IMF driving conditions (Murr & Hughes, 2001). This will generally mean that statistical Poynting fluxes during southward (northward) IMF orientations are slight underestimations (overestimations) because they include values calculated during variable IMF conditions.

### 2.2.1. Electric Field

The SuperDARN (Chisham et al., 2007; Greenwald et al., 1995; Nishitani et al., 2019) consists of 36 (as of 2020) high-frequency radars in both the northern and southern hemispheres. Line-of-sight doppler velocities of the F-region (~250 km altitude) plasma are measured by each radar within a large field-of-view spanning a few thousand kilometers, which are then all gridded together based on hemisphere. A spherical harmonic fit (Ruohoniemi & Greenwald, 1996) is applied to the gridded velocities to solve for the instantaneous global electrostatic potential,  $\Phi$ , which is related to the ionospheric electric field by  $\mathbf{E} = -\nabla\Phi$ . Using the electric potential solution, the full electric field vector can be calculated at any position in a hemisphere, which is what was done for each grid cell used for the CHAMP data binning. When using SuperDARN data in this way, it is also common to employ an empirical electric potential model (e.g., Thomas & Shepherd, 2018) that is based on the IMF to “fill in the gaps” for regions where SuperDARN velocity data is scarce. This however can potentially introduce occasions where the global maps of  $\Phi$  are very dependent on the empirical model if there is not enough input data. In this study, we have utilized the Thomas and Shepherd (2018) model in the 2-min resolution maps of electric potential that were used, but only during times where 200 or more gridded SuperDARN data points were available in the map. This means that only maps with a significant amount of measured data constraining the spherical harmonic fit to  $\Phi$  were included. Two hundred points is generally good enough to ensure a reasonable spread of data globally, whilst reducing the amount of “usable” 2-min maps by around 55% (Billett et al., 2018). It should be noted that due to the nature of using a global fit, there will undoubtedly be occasional regions of spurious electric electric fields where data may be sparse, which will then increase the error in the subsequent Poynting flux calculation. The 200 gridded data point threshold minimizes that error, but will not entirely eliminate it. The ubiquity of SuperDARN data in certain local times does however vary with universal time, so the error caused by data sparseness will “average out” across all local times when Poynting fluxes are eventually averaged.

### 2.2.2. Perturbation Magnetic Field

The AMPERE (Anderson et al., 2014) uses magnetometers on board the Iridium satellite constellation to derive global maps of both the northern and southern hemisphere FACs. The in-situ magnetic field at around 780 km altitude is sampled, then perturbations caused by FACs ( $\delta\mathbf{B}$ ) are determined by subtracting the Earth’s intrinsic magnetic field using the IGRF model (Thébault et al., 2015). Further corrections are then made to account for various sensor biases, residuals and noise (Anderson et al., 2000), and a spherical harmonic fit is then applied to provide perturbations at every local time and latitude. Finally, the fitted data

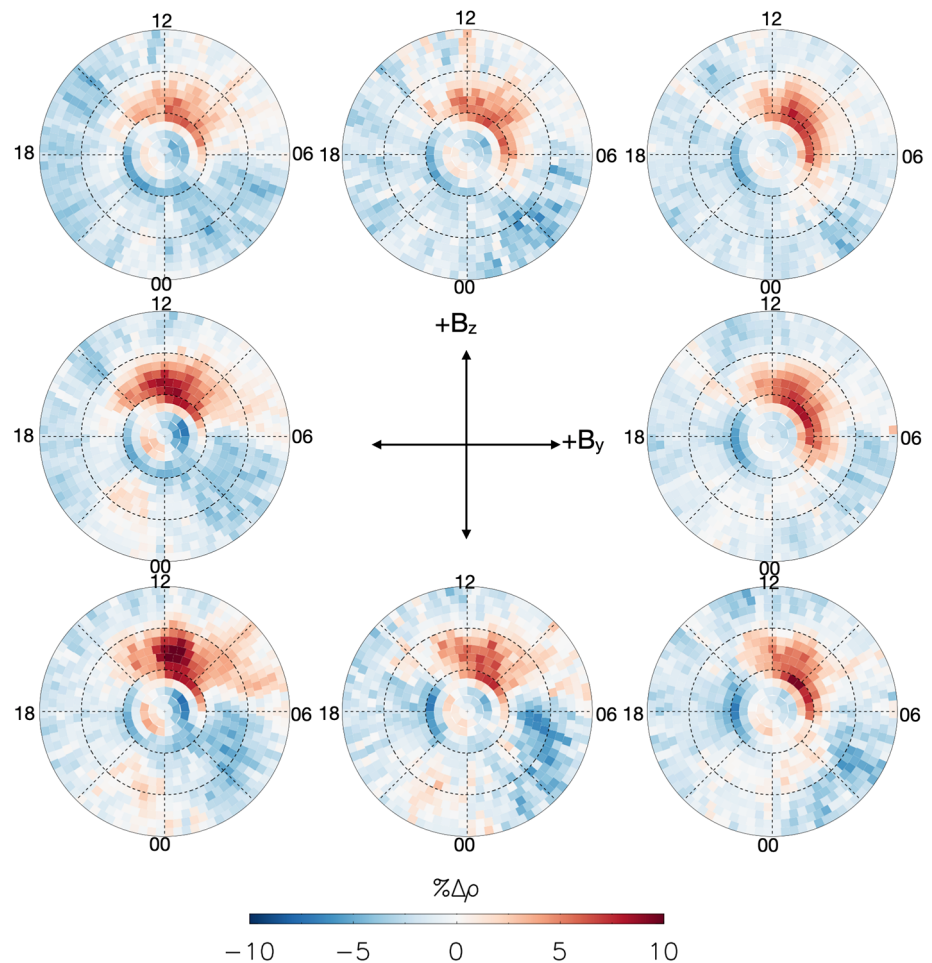


**Figure 2.** Average perturbation neutral densities ( $\Delta\rho$ ) for the entirety of the CHAMP neutral mass density data set, in the same format as Figure 1. CHAMP, Challenging Minisatellite Payload.

values are normalized to an altitude of 250 km (to match the assumed altitude of SuperDARN measurements; Yeoman et al., 2008) to account for the convergence of magnetic field lines with decreasing altitude (using the  $3/2$  relationship described by Knipp et al., 2014). Similarly to the SuperDARN derived electric fields, the AMPERE spherical harmonic fitting processes induces some small error when determining Poynting flux in regions where the Iridium satellites are further apart. This is due to their orbit inclination being offset from the magnetic pole, causing uneven spatial coverage with respect to magnetic coordinates.

$\delta\mathbf{B}$  is gridded with respect to AACGM coordinates spaced  $1^\circ$  in latitude and 1 h ( $15^\circ$ ) of MLT, with a time resolution of 2 min and integration window of 10 min. Subsequently binning the magnetic perturbations onto the same grid used for the CHAMP data involved iterating over each AMPERE grid cell, then binning each data point onto every overlapping CHAMP grid cell. Cells with two or more  $\delta\mathbf{B}$  were then averaged over each timestep.

### 3. Results

Figure 2 shows the average perturbation neutral density ( $\Delta\rho$ ) patterns for 8 IMF clock angle orientations, derived using Equation 1 and the entirety of the CHAMP data set above  $60^\circ$  AACGM latitude. Immediately noticeable under all IMF orientations is a positive enhancement of several percent above the background neutral density in the region between  $70\text{--}80^\circ$  MLat and  $7\text{--}14$  MLT. The enhancement looks to be slightly smaller under positive  $B_z$  conditions, and there is a  $B_y$  dependence on its asymmetry around magnetic local

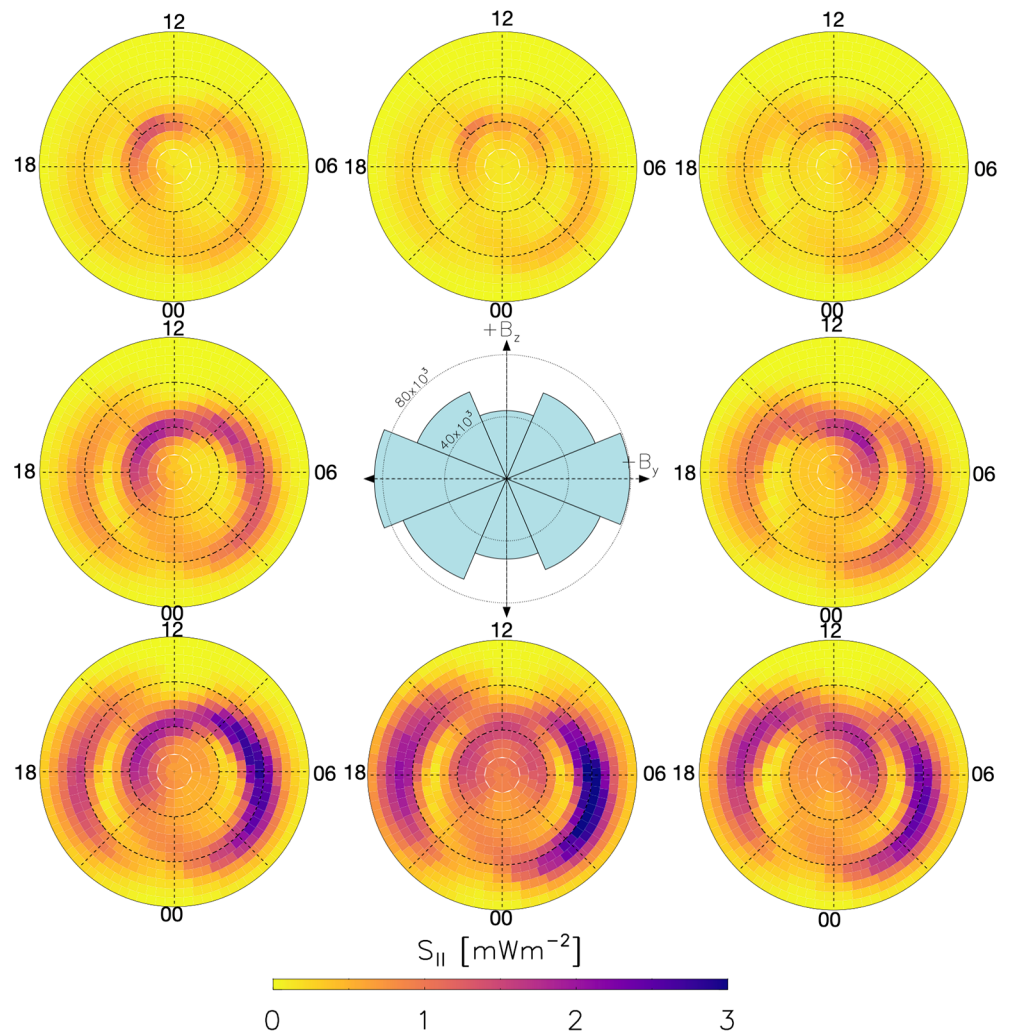


**Figure 3.** Average Poynting flux ( $S_{||}$ ) calculated using AMPERE perturbation magnetic fields and SuperDARN electric fields between 2010 and 2017, in the same format as Figure 2. Only positive values are shown (downward flux), because negative (upward) fluxes were minuscule on average compared to the positive values. The center IMF dial also shows the number of Poynting flux maps that went into each average, marked with indicator circles at  $40 \times 10^3$  and  $80 \times 10^3$  maps. AMPERE, Active Magnetosphere and Planetary Electrodynamics Response Experiment; IMF, interplanetary magnetic field; SuperDARN, Super Dual Auroral Radar Network.

noon. The enhancement extends from approximately 5–13 MLT for positive  $B_y$ , and from 8 to 15 MLT for negative  $B_y$  conditions.

For all patterns of  $\Delta\rho$ , there is a depletion region between 1 and 6 MLT, encompassing anywhere from  $\sim 10$  to  $25^\circ$  of latitudinal width depending on the IMF orientation. The latitudinal extent of the depletion appears to also have a  $B_y$  dependence, where positive values show a latitudinally thinner region. This might explain why the depletion for the purely  $B_y$  positive pattern is much weaker than the others, such that it is more difficult to pick out from the surrounding areas. For patterns where  $B_z$  is negative, there is an additional moderate  $\Delta\rho$  depletion around  $80^\circ$  MLat centered on magnetic local dusk. In all other regions for all patterns,  $\Delta\rho$  has a low magnitude on average compared to the more distinct regions just described.

Figure 3 shows the average Poynting flux ( $S_{||}$ ) patterns derived using Equation 2 with SuperDARN and AMPERE data. It is important to note here that the CHAMP data set (2000–2010) does not overlap with the AMPERE data set (2010–2017), therefore the  $S_{||}$  and  $\Delta\rho$  averages are calculated from different timespans. Both however are calculated from  $\sim 10$  to  $\sim 7$  years worth of data, respectively, thus should give accurate statistical representations. The number of 2-min Poynting flux maps which were used in the averaging for

each statistical pattern are shown in the center of Figure 3, ranging from a minimum of  $\sim 45 \times 10^3$  maps to a maximum  $\sim 85 \times 10^3$  maps used, depending on IMF orientation. Negative (upward) Poynting fluxes have also not been shown in Figure 3 because their magnitude, on average, is exceedingly small compared to positive values in all regions (i.e., downward into the ionosphere). This is because on average it would be expected, and is clearly apparent in our results, that the magnetosphere drives the ionosphere and not vice versa (Gary et al., 1995). Upward Poynting flux is still an occasional occurrence in localized regions of the ionosphere, which will have introduced slight biases towards lower magnitudes in Figure 3 averages. Upward Poynting fluxes in the cusp region are however not common (Gary et al., 1995), and so should not significantly affect the results presented here.

Larger than surrounding area values are seen in the high-latitude  $\sim 78\text{--}82^\circ$  MLat dayside region for all patterns (which we henceforth refer to as the cusp region), the local time extent of which is highly controlled by the IMF  $B_y$  component. The  $B_y$  positive patterns have a strong cusp region enhancement that is shifted towards dawn, whilst the enhancement under  $B_y$  negative patterns is shifted towards dusk. For all  $S_{\parallel}$  patterns in Figure 3, enhancements of downward flux are also seen on both the dawn and dusk sides between  $60$  and  $75^\circ$  MLat, the dawnside enhancements being consistently stronger for all IMF orientations. Overall magnitudes of  $S_{\parallel}$  are much greater for the negative IMF  $B_z$  patterns in general when compared to positive  $B_z$ , and the aforementioned dawn and dusk enhancements extend to lower latitudes under negative  $B_z$  conditions.

#### 4. Discussion

Our statistical patterns of the perturbation neutral mass density,  $\Delta\rho$ , shown in Figure 2 clearly show the cusp neutral density enhancement. Although as it is observable during both geomagnetically quiet and active times (H. Liu et al., 2005; Kwak et al., 2009), this is not a particularly surprising result. Both Yamazaki et al. (2015a, 2015b) showed very similar results, but expressed their neutral densities as perturbations from a quiet time state. Our values in contrast include both quiet and active times, showing that the neutral density in the cusp region is always enhanced by several percent above the surrounding regions, for all IMF orientations and magnitudes. It is also worth mentioning that the negative neutral density perturbation in the dawnside region we show is a well-known thermospheric feature that is thought to be caused by downward winds, in response to a traditional cyclonic plasma convection cell on the dawnside (Crowley et al., 1996; Guo et al., 2019). It was originally predicted by the Crowley et al. (1996) model that the dawnside depletion would not be detectable at CHAMP altitudes. Previous studies involving CHAMP data however, including ours, do show its existence. Schlegel et al. (2005) hypothesized that the discrepancy might be caused by either imperfect upper boundary conditions, or the non-inclusion of wave motions within the model.

A key similarity our results share with the studies previously mentioned is that under northward IMF  $B_z$  conditions, the cusp enhancement is still a prominent feature of the high-latitude thermosphere. The absolute magnitude of the neutral mass density is lower in the cusp region when the IMF  $B_z$  is positive (e.g., Yamazaki et al., 2015a), but a new observation from these results is that the percentage density enhancement above background levels is relatively consistent across all IMF orientations.

When discussing neutral mass density perturbations sorted by IMF orientation, such as those shown in Figure 2, it is also important to consider the timescales upon which the thermosphere takes to respond to a change in ionospheric conditions. For example, if several hours of southward orientated IMF causes a neutral mass density perturbation, and then the IMF turns northward, the density could stay enhanced for several hours as it gradually returns to the background level (Qian & Solomon, 2012). The presence of the cusp mass density perturbation during occasions of northward IMF could therefore be further enhanced due to previous forcing conditions, rather than current conditions. It was mentioned previously in Section 2.1 that an IMF “steadiness” filter of a few minutes did not modify the  $\Delta\rho$  averages, but significantly reduced the amount of data used (a  $\sim 50\%$  reduction in usable data when filtering for 20 min long steady IMF conditions). In order to potentially remove the impact of past conditions on the results in Figure 2, an IMF steadiness filter on the order of hours would be required, which would leave very few events to be used in averaging. This perhaps offers an explanation for why the cusp neutral mass density enhancement seems to exist for all IMF orientations in this and past studies (e.g., H. Liu et al., 2005).



The SuperDARN/AMPERE statistical patterns of downward Poynting flux in Figure 3 are consistent with previous modeling and observational results (e.g., Cosgrove et al., 2014; Deng & Ridley, 2007; McHarg et al., 2005; Weimer, 2005; Zhang et al., 2005), that is, distinct regions of high downward flux on the dawn and dusk sides where the convection electric field, and thus Joule heating, is high. Many of these studies have also shown patterns binned by IMF orientation that displayed a very large decrease in downward Poynting flux magnitude over the entire hemisphere when  $B_z$  is positive compared to negative, in agreement with our results. Figure 3 also shows that downward Poynting flux is higher on the dawnside compared to the duskside below  $\sim 75^\circ$  MLat, which is consistent with enhanced dawnside Joule heating due to neutral winds opposing the direction of plasma convection (Billett et al., 2018). It is not surprising that every pattern in Figure 3 has a perceptible cusp region Poynting flux enhancement above background levels, as Milan et al. (1998) showed that the F-region dayside cusp is a “hard target” for the SuperDARN radars, meaning it is commonly observable regardless of changing ionospheric conditions.

The empirical Poynting flux model by Cosgrove et al. (2014) shows the cusp to be an important feature under northward IMF conditions. Cosgrove et al. (2014) attributed this deviation from previous studies as an indication of electric field variability in the cusp region which could not be captured with empirical models. Electric field measurements from the SuperDARN used in this study were however not averaged; each individual 2-min integrated electric field map was paired with a perturbation magnetic field map from AMPERE to derive an instantaneous global Poynting flux map. Therefore, the variability of the electric field that the SuperDARN map fitting process calculates is preserved. There is a degree of “smoothing out” of the electric potential spatially when the spherical harmonic fit is applied to radar velocity data, but this does not affect the SuperDARNs ability to detect small temporal electric field variability on the order of minutes (Cousins & Shepherd, 2012a, 2012b).

The IMF  $B_z$  positive patterns in Figure 3 do indeed show that downward Poynting flux in the cusp region is higher than that in the  $60\text{--}75^\circ$  MLat dawn and dusk regions (i.e., the auroral zone), whilst the opposite is true when  $B_z$  is negative. This is in general agreement with the Cosgrove et al. (2014) model, although the magnitudes shown here are not as large. Downward Poynting fluxes in the cusp region during northward IMF are highly sensitive to the IMF magnitude (Li et al., 2011; Lu et al., 2018), which could mean the averages shown in Figure 3 are weighted down by Poynting flux patterns with low IMF magnitudes. Additionally, the Cosgrove et al. (2014) model utilizes significantly finer time resolution electric field measurements than those used in this study ( $<0.25$  s vs. 2 min), which could potentially have resolved electric fields associated with the fine-scale FACs that Lühr et al. (2004) saw alongside the cusp density enhancement originally. The bin sizes used for our statistical patterns are also very much within the region of mesoscales ( $\sim 100$ s of square kilometers in area), so they would not resolve the effects of small and fine-scale phenomena.

To better compare our results of Poynting flux enhancements and neutral mass density perturbations in the cusp region, Figure 4 shows all binned values of  $S_{\parallel}$  (black) and  $\Delta\rho$  (red) between MLTs of 11–13 and AACGM latitudes of  $60\text{--}90^\circ$ , for each IMF orientation. The MLT range was chosen to be 2 h wide around magnetic local noon to isolate the cusp region, but also so that large Poynting fluxes from the dawn and dusk side enhancement regions (seen for all patterns in Figure 3) were not introduced.

$\Delta\rho$  peaks at AACGM latitudes as low as  $75^\circ$  (bottom right plot) and as high as  $81^\circ$  (top right plot), which is very consistent with the cusp neutral mass density enhancement locations seen by Lühr et al. (2004) and later authors. There is also a high-latitude peak of  $S_{\parallel}$  that is distinct and near the  $\Delta\rho$  peaks for most IMF orientations. In general, downward Poynting flux appears to maximize  $2\text{--}4^\circ$  poleward of neutral mass density perturbations in latitude, being closest when the IMF  $B_y$  is positive.

It is interesting to see in Figure 4 that even though peaks in  $S_{\parallel}$  occur approximately in a similar region to peaks in  $\Delta\rho$ , their magnitudes do not appear closely correlated. For example, the cusp peak of  $\Delta\rho$  is approximately the same when  $B_z$  is both positive and negative (with zero  $B_y$ ), but the Poynting flux is larger by around a factor of two when the IMF is southward compared to northward. This might be because a short term (10s of minutes) injection of downward Poynting flux near the cusp would result in the neutral density in the same region to become enhanced for several hours (e.g., Sutton et al., 2009; Wang et al., 2020). The discrepancy between how short a time the Poynting flux is enhanced and how long the neutral mass density is enhanced would cause the patterns of  $\Delta\rho$  to be biased towards strong geomagnetic events, whilst  $S_{\parallel}$  would

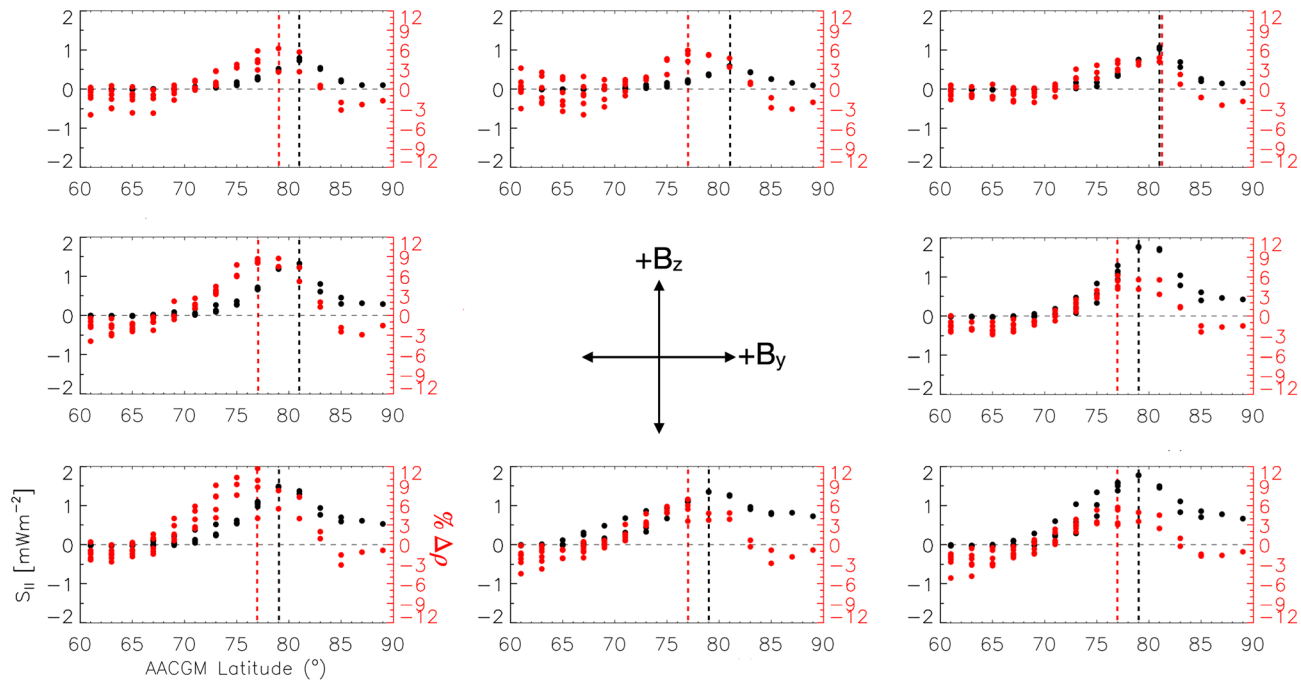


**Figure 4.** Binned values of  $\Delta\rho$  (red) and  $S_{||}$  (black) from Figures 2 and 3 between 11–13 MLT and 60–90° AACGM latitude. Red and black dotted lines denote the AACGM latitude of maximum  $\Delta\rho$  and  $S_{||}$ , respectively. AACGM, altitude-adjusted corrected geomagnetic coordinates; MLT, magnetic local time.

be biased towards quiet geomagnetic times which are more frequent than large events such as those seen by Crowley et al. (2010) and Knipp et al. (2011).

We also note that  $\Delta\rho$  is larger in the cusp region when the IMF  $B_y$  is negative compared to positive, but  $S_{||}$  is of a similar magnitude when  $B_y$  is both positive and negative (for the same  $B_z$ ). Yamazaki et al. (2015a) saw the same neutral density asymmetry in their results, but focused mainly on discussing its effect on the dawnside density depletion region (also seen in Figure 3). It is clear that both  $\Delta\rho$  and  $S_{||}$  in the cusp region have a significant local time dependency on  $B_y$  (e.g., in Figures 2 and 3), but the local time extent of cusp enhancements, in addition to the magnitudes, do not correlate well. For example, cusp region  $S_{||}$  extends much further onto the duskside during  $B_y$  negative conditions, but the corresponding  $\Delta\rho$  pattern is fairly symmetric around noon. If enhanced downward Poynting fluxes were indeed a 1:1 correlation with enhanced neutral densities on these spatial scales, then co-rotation of thermospheric neutrals would cause density perturbations much further onto the duskside than is seen in Figure 2 for negative  $B_y$  patterns.

As  $\Delta\rho$  is in terms of the neutral mass density in surrounding areas, it is reasonable to interpret any cusp perturbation to be due to solar wind energy input variations and not due to “background processes” that affect the density such as solar EUV dissociation/recombination. Our calculations of the Poynting flux based on SuperDARN and AMPERE data however do not totally explain the cusp density enhancement based on magnitude alone, also factoring the bias in  $\Delta\rho$  towards strong events. This could be because fine scale FAC structures such as those initially seen by Lühr et al. (2004) can be filtered out in the AMPERE and SuperDARN global fitting procedures. Variable cusp region electric fields are however sometimes apparent in the line-of-sight velocity and spectral width data products of individual SuperDARN radars (e.g., Baker et al., 1995; Nishitani et al., 1999; Pinnock et al., 1995). The mesoscale downward Poynting flux averages captured by our patterns (on the order of  $\sim 1,000$  km spatial resolution) indicate that enhancements in the general cusp region are at least common enough to be statistically significant, but are perhaps not the main driver behind neutral mass density enhancements on a similar scale. Alternatively, it could be a result of the vastly different response timescales between the thermosphere and ionosphere that causes  $\Delta\rho$  and  $S_{||}$  to appear not well correlated statistically.

The altitudinal dependence of Poynting flux deposition in the thermosphere is an important factor that is not considered in our analysis. We effectively only show the total altitude integrated downward Poynting flux, as both the SuperDARN velocities and AMPERE magnetic field measurements used are from F-region altitudes (>250 km). Most of the energy included in our statistical averages will be deposited at E-region altitudes where the Pedersen conductivity is high, but it has been shown that the smaller amount of energy deposition in the F-region is enough to drive thermospheric upwelling and winds at the same altitude due to soft particle precipitation and low neutral densities (Billett et al., 2020; Brinkman et al., 2016; Clemmons et al., 2008; Deng et al., 2011). This may account for the lack of correlation between our estimated Poynting flux deposited in E-region and cusp neutral mass density enhancements at CHAMP altitudes (~400 km). We cannot make a conclusion as to the mechanism by which mesoscale downward Poynting flux contributes to mesoscale neutral density perturbations, but as the height-integrated averages shown in this study are mostly dissipated in the E region, it perhaps contributes most to the temporal variation of the cusp neutral density via vertical acoustic wave propagation, as per the modeling results by Deng et al. (2011) showing that to be the case.

## 5. Summary

Using the CHAMP data set, we have produced statistical patterns of the perturbation neutral mass density based on IMF orientation. Our technique is novel, as the perturbations are expressed as a percentage of the instantaneous background neutral mass density for each CHAMP orbit. We have also for the first time generated statistical patterns of the total downward Poynting flux into the atmosphere utilizing the combined SuperDARN and AMPERE datasets, from the technique described originally by Waters et al. (2004). The well-known dayside cusp neutral density enhancement was examined on mesoscales and compared to the calculated Poynting flux. It was found that:

- Neutral mass density perturbations of several percent above background levels exist in the dayside cusp regions for all orientations of the IMF. The perturbation above the background density is larger when the IMF  $B_y$  is negative.
- There is an enhancement of the total downward Poynting flux in the cusp region for all orientations of the IMF, but it is considerably higher globally when the IMF  $B_z$  is negative. Under positive  $B_z$  conditions, downward Poynting flux in the cusp is higher than that in the lower latitude auroral zone. The local time maximum of cusp region Poynting flux is highly dependent on the IMF  $B_y$ .
- Total downward Poynting fluxes at mesoscales on average do not appear to fully correlate with average neutral mass density perturbations on the same scale, for example, the morphology and magnitude differences between patterns for different IMF orientations. The lack of correlation gives valuable insights to alternative processes which may be the primary cause of the cusp density perturbations.

It is clear from our results and comparisons with previous studies and empirical models that using the AMPERE and SuperDARN datasets in this way to derive global patterns of total Poynting flux is powerful. In the cusp region, there is a notable enhancement of the average downward Poynting flux, but there is a lack of correlation with the neutral mass density enhancements measured by CHAMP in the same region and on the same spatial scale. This means that other important processes at play may account for the discrepancy, for example, FACs that occur on a smaller scale than the SuperDARN-AMPERE observations, or soft particle precipitation at lower F-region altitudes causing neutral particle upwelling to CHAMP altitudes. An additional effect that could have an impact is the response timescales of enhanced Poynting flux to the onset of active ionospheric conditions, which are likely significantly shorter than timescales for enhanced neutral mass densities.

There is scope to further utilize the SuperDARN-AMPERE method to examine Poynting flux on a global scale, such as to estimate the morphology and magnitude of Joule heating during case studies, but it would also be possible to increase the spatial resolution substantially in a localized region by using data from individual SuperDARN radars and Iridium satellites.

## Data Availability Statement

The authors acknowledge the use of data from SuperDARN, an international project made possible by the national funding agencies of Australia, Canada, China, France, Italy, Japan, South Africa, Norway, the United Kingdom, and the United States of America. SuperDARN data can be downloaded from Globus, instructions of which are provided here: <https://superdarn.ca/data-products>. SuperDARN data in this study was processed using the Radar Software Toolkit (RST), version 4.3: <https://github.com/SuperDARN/rst>. We also thank the AMPERE team and the AMPERE Science Center for providing the Iridium derived data products, which can be plotted and downloaded at: <http://ampere.jhuapl.edu/>. CHAMP pre-processed neutral density measurements and positional information was obtained from the GFZ Potsdam data repository at <http://doi.org/10.5880/GFZ.1.1.2019.001>.

## Acknowledgments

This work was, in part, developed out of a collaborative effort between the students of the CHAMPERE group and the instructors of the first CaNoRock STEP program, which took place in November, 2013, at Barrier Lake Station, Kananaskis, Alberta. The authors thank the Barrier Lake Station staff for their hospitality. The research was supported by both the National Sciences and Engineering Research Council of Canada (NSERC) and the Norwegian Centre for International Cooperation in Education (SiU) project NNA-2012/10099. D. D. Billett was supported by NSERC CREATE Grant #479771-20, K. A. McWilliams was supported by NSERC Discovery Grant #RGPIN 05472-2017 and J. P. Reistad was funded by the Norwegian Research Council through grant 300844/F50. The authors also thank D. Knudsen and J.-P. St-Maurice for their valuable input and discussions.

## References

- Anderson, B. J., Korth, H., Waters, C. L., Green, D. L., Merkin, V. G., Barnes, R. J., & Dyrud, L. P. (2014). Development of large-scale Birkeland currents determined from the Active Magnetosphere and Planetary Electrodynamics Response Experiment. *Geophysical Research Letters*, *41*(9), 3017–3025. <https://doi.org/10.1002/2014gl059941>
- Anderson, B. J., Takahashi, K., & Toth, B. A. (2000). Sensing global Birkeland currents with iridium engineering magnetometer data. *Geophysical Research Letters*, *27*(24), 4045–4048. <https://doi.org/10.1029/2000gl000094>
- Baker, K. B., Dudeney, J. R., Greenwald, R. A., Pinnock, M., Newell, P. T., Rodger, A. S., et al. (1995). HF radar signatures of the cusp and low-latitude boundary layer. *Journal of Geophysical Research*, *100*(A5), 7671–7695. <https://doi.org/10.1029/94ja01481>
- Billett, D. D., Grocott, A., Wild, J. A., Walach, M.-T., & Kosch, M. J. (2018). Diurnal variations in global Joule heating morphology and magnitude due to neutral winds. *Journal of Geophysical Research: Space Physics*, *123*(3), 2398–2411
- Billett, D. D., McWilliams, K. A., & Conde, M. G. (2020). Colocated observations of the E and F region thermosphere during a substorm. *Journal of Geophysical Research: Space Physics*, *125*(11), e2020JA028165. <https://doi.org/10.1029/2020ja028165>
- Brinkman, D. G., Walterscheid, R. L., Clemmons, J. H., & Hecht, J. H. (2016). High-resolution modeling of the cusp density anomaly: Response to particle and Joule heating under typical conditions. *Journal of Geophysical Research: Space Physics*, *121*(3), 2645–2661. <https://doi.org/10.1002/2015ja021658>
- Chisham, G., Lester, M., Milan, S. E., Freeman, M. P., Bristow, W. A., Grocott, A., et al. (2007). A decade of the Super Dual Auroral Radar Network (SuperDARN): Scientific achievements, new techniques and future directions. *Surveys in Geophysics*, *28*(1), 33–109. <https://doi.org/10.1007/s10712-007-9017-8>
- Clemmons, J. H., Friesen, L. M., Katz, N., Ben-Ami, M., Dotan, Y., & Bishop, R. L. (2009). The ionization gauge investigation for the Streak mission. *Space Science Reviews*, *145*(3–4), 263–283. <https://doi.org/10.1007/s11214-009-9489-6>
- Clemmons, J. H., Hecht, J. H., Salem, D. R., & Strickland, D. J. (2008). Thermospheric density in the Earth's magnetic cusp as observed by the Streak mission. *Geophysical Research Letters*, *35*(24). <https://doi.org/10.1029/2008GL035972>
- Codrescu, M. V., Fuller-Rowell, T. J., & Foster, J. C. (1995). On the importance of E-field variability for Joule heating in the high-latitude thermosphere. *Geophysical Research Letters*, *22*(17), 2393–2396. <https://doi.org/10.1029/95gl01909>
- Cosgrove, R. B., Bahcivan, H., Chen, S., Strangeway, R. J., Ortega, J., Alhassan, M., et al. (2014). Empirical model of Poynting flux derived from FAST data and a cusp signature. *Journal of Geophysical Research: Space Physics*, *119*(1), 411–430. <https://doi.org/10.1002/2013ja019105>
- Cosgrove, R. B., & Thayer, J. P. (2006). Parametric dependence of electric field variability in the Sondrestrom database: A linear relation with Kp. *Journal of Geophysical Research: Space Physics*, *111*(A10). <https://doi.org/10.1029/2006ja011658>
- Cousins, E. D. P., & Shepherd, S. G. (2012a). Statistical characteristics of small-scale spatial and temporal electric field variability in the high-latitude ionosphere. *Journal of Geophysical Research: Space Physics*, *117*(A3). <https://doi.org/10.1029/2011ja017383>
- Cousins, E. D. P., & Shepherd, S. G. (2012b). Statistical maps of small-scale electric field variability in the high-latitude ionosphere. *Journal of Geophysical Research: Space Physics*, *117*(A12). <https://doi.org/10.1029/2012ja017929>
- Crowley, G., Knipp, D. J., Drake, K. A., Lei, J., Sutton, E., & Lühr, H. (2010). Thermospheric density enhancements in the dayside cusp region during strong BY conditions. *Geophysical Research Letters*, *37*(7). <https://doi.org/10.1029/2009gl042143>
- Crowley, G., Schoendorf, J., Roble, R. G., & Marcos, F. A. (1996). Cellular structures in the high-latitude thermosphere. *Journal of Geophysical Research*, *101*(A1), 211–223. <https://doi.org/10.1029/95JA02584>
- Demars, H. G., & Schunk, R. W. (2007). Thermospheric response to ion heating in the dayside cusp. *Journal of Atmospheric and Solar-Terrestrial Physics*, *69*(6), 649–660. <https://doi.org/10.1016/j.jastp.2006.11.002>
- Deng, Y., Fuller-Rowell, T. J., Akmaev, R. A., & Ridley, A. J. (2011). Impact of the altitudinal Joule heating distribution on the thermosphere. *Journal of Geophysical Research: Space Physics*, *116*(A5). <https://doi.org/10.1029/2010ja016019>
- Deng, Y., Fuller-Rowell, T. J., Ridley, A. J., Knipp, D., & Lopez, R. E. (2013). Theoretical study: Influence of different energy sources on the cusp neutral density enhancement. *Journal of Geophysical Research: Space Physics*, *118*(5), 2340–2349. <https://doi.org/10.1002/jgra.50197>
- Deng, Y., & Ridley, A. J. (2007). Possible reasons for underestimating Joule heating in global models: E field variability, spatial resolution, and vertical velocity. *Journal of Geophysical Research: Space Physics*, *112*(A9). <https://doi.org/10.1029/2006ja012006>
- Doornbos, E., Van Den Ijssel, J., Luhr, H., Forster, M., & Koppenwallner, G. (2010). Neutral density and crosswind determination from arbitrarily oriented multi-axis accelerometers on satellites. *Journal of Spacecraft and Rockets*, *47*(4), 580–589. <https://doi.org/10.2514/1.48114>
- Förster, M., & Doornbos, E. (2019). Upper thermosphere neutral wind cross-track component deduced from CHAMP accelerometer data. <https://doi.org/10.5880/GFZ.1.1.2019.001>
- Förster, M., Paschmann, G., Haaland, S. E., Quinn, J. M., Torbert, R. B., Vaith, H., & Kletzing, C. A. (2007). High-latitude plasma convection from Cluster EDI: variances and solar wind correlations. *Annals of Geophysics*, *25*(7), 1691–1707. <https://doi.org/10.5194/angeo-25-1691-2007>
- Gary, J. B., Heelis, R. A., & Thayer, J. P. (1995). Summary of field-aligned Poynting flux observations from DE 2. *Geophysical Research Letters*, *22*(14), 1861–1864. <https://doi.org/10.1029/95gl00570>



- Greenwald, R. A., Baker, K. B., Dudeney, J. R., Pinnock, M., Jones, T. B., Thomas, E. C., et al. (1995). DARN/SuperDARN. *Space Science Reviews*, 71(1-4), 761–796. <https://doi.org/10.1007/BF00751350>
- Guo, D., Lei, J., Ridley, A., & Ren, D. (2019). Low-density cell of the thermosphere at high latitudes revisited. *Journal of Geophysical Research: Space Physics*, 124(1), 521–533. <https://doi.org/10.1029/2018JA025770>
- Haaland, S. E., Paschmann, G., Förster, M., Quinn, J. M., Torbert, R. B., McIlwain, C. E., et al. (2007). High-latitude plasma convection from Cluster EDI measurements: method and IMF-dependence. *Annals of Geophysics*, 25(1), 239–253. <https://doi.org/10.5194/angeo-25-239-2007>
- King, J. H., & Papitashvili, N. E. (2005). Solar wind spatial scales in and comparisons of hourly Wind and ACE plasma and magnetic field data. *Journal of Geophysical Research: Space Physics*, 110(A2). <https://doi.org/10.1029/2004ja010649>
- Knipp, D. J., Eriksson, S., Kilcommons, L., Crowley, G., Lei, J., Hairston, M., & Drake, K. (2011). Extreme Poynting flux in the dayside thermosphere: Examples and statistics. *Geophysical Research Letters*, 38(16). <https://doi.org/10.1029/2011gl048302>
- Knipp, D. J., Matsuo, T., Kilcommons, L., Richmond, A., Anderson, B., Korth, H., et al. (2014). Comparison of magnetic perturbation data from LEO satellite constellations: Statistics of DMSP and AMPERE. *Space Weather*, 12(1), 2–23. <https://doi.org/10.1002/2013sw000987>
- Kwak, Y.-S., Richmond, A. D., Deng, Y., Forbes, J. M., & Kim, K.-H. (2009). Dependence of the high-latitude thermospheric densities on the interplanetary magnetic field. *Journal of Geophysical Research: Space Physics*, 114(A5). <https://doi.org/10.1029/2008ja013882>
- Li, W., Knipp, D. J., Lei, J., & Raeder, J. (2011). The relation between dayside local Poynting flux enhancement and cusp reconnection. *Journal of Geophysical Research: Space Physics*, 116(A8). <https://doi.org/10.1029/2011ja016566>
- Liu, H., Lühr, H., Henize, V., & Köhler, W. (2005). Global distribution of the thermospheric total mass density derived from CHAMP. *Journal of Geophysical Research: Space Physics*, 110(A4). <https://doi.org/10.1029/2004ja010741>
- Liu, R., Lühr, H., & Ma, S.-Y. (2010). Storm-time related mass density anomalies in the polar cap as observed by CHAMP. *Annals of Geophysics*, 28, 165–180. <https://doi.org/10.5194/angeo-28-165-2010>
- Lu, Y., Deng, Y., Sheng, C., Kilcommons, L., & Knipp, D. J. (2018). Poynting flux in the dayside polar cap boundary regions from DMSP F15 satellite measurements. *Journal of Geophysical Research: Space Physics*, 123(8), 6948–6956. <https://doi.org/10.1029/2018ja025309>
- Lühr, H., Rother, M., Köhler, W., Ritter, P., & Grunwaldt, L. (2004). Thermospheric up-welling in the cusp region: Evidence from CHAMP observations. *Geophysical Research Letters*, 31(6). <https://doi.org/10.1029/2003gl019314>
- McHarg, M., Chun, F., Knipp, D., Lu, G., Emery, B., & Ridley, A. (2005). High-latitude Joule heating response to IMF inputs. *Journal of Geophysical Research: Space Physics*, 110(A8). <https://doi.org/10.1029/2004ja010949>
- McWilliams, L. B. N., Milan, S. E., & Grocott, A. (2014). Thermospheric density perturbations in response to substorms. *Journal of Geophysical Research: Space Physics*, 119(6), 4441–4455. <https://doi.org/10.1002/2014ja019837>
- Milan, S. E., Yeoman, T. K., & Lester, M. (1998). The dayside auroral zone as a hard target for coherent HF radars. *Geophysical Research Letters*, 25(19), 3717–3720. <https://doi.org/10.1029/98gl02781>
- Moe, K., & Moe, M. M. (2008). The high-latitude thermospheric mass density anomaly: A historical review and a semi-empirical model. *Journal of Atmospheric and Solar-Terrestrial Physics*, 70(5), 794–802. <https://doi.org/10.1016/j.jastp.2007.10.007>
- Murr, D. L., & Hughes, W. J. (2001). Reconfiguration timescales of ionospheric convection. *Geophysical Research Letters*, 28(11), 2145–2148. <https://doi.org/10.1029/2000gl012765>
- Nishitani, N., Ogawa, T., Pinnock, M., Freeman, M. P., Dudeney, J. R., Villain, J.-P., et al. (1999). A very large scale flow burst observed by the SuperDARN radars. *Journal of Geophysical Research*, 104(A10), 22469–22486. <https://doi.org/10.1029/1999ja000241>
- Nishitani, N., Ruohoniemi, J. M., Lester, M., Baker, J. B. H., Koustov, A. V., Shepherd, S. G., et al. (2019). Review of the accomplishments of mid-latitude Super Dual Auroral Radar Network (SuperDARN) HF radars. *Progress in Earth and Planetary Science*, 6(1). <https://doi.org/10.1186/s40645-019-0270-5>
- Pinnock, M., Rodger, A. S., Dudeney, J. R., Rich, F., & Baker, K. B. (1995). High spatial and temporal resolution observations of the ionospheric cusp. *Annals of Geophysics*, 13, 919–925. <https://doi.org/10.1007/s00585-995-0919-9>
- Pröls, G. W. (2011). Density perturbations in the upper atmosphere caused by the dissipation of solar wind energy. *Surveys in Geophysics*, 32(2), 101–195. <https://doi.org/10.1007/s10712-010-9104-0>
- Qian, L., & Solomon, S. C. (2012). Thermospheric density: An overview of temporal and spatial variations. *Space Science Reviews*, 168(1-4), 147–173. <https://doi.org/10.1007/s11214-011-9810-z>
- Reigber, C., Lühr, H., & Schwintzer, P. (2002). CHAMP mission status. *Advances in Space Research*, 30(2), 129–134. [https://doi.org/10.1016/s0273-1177\(02\)00276-4](https://doi.org/10.1016/s0273-1177(02)00276-4)
- Rentz, S., & Lühr, H. (2008). Climatology of the cusp-related thermospheric mass density anomaly, as derived from CHAMP observations. *Annals of Geophysics*, 26, 2807–2823. <https://doi.org/10.5194/angeo-26-2807-2008>
- Richmond, A. D. (1992). Assimilative mapping of ionospheric electrodynamics. *Advances in Space Research*, 12(6), 59–68. [https://doi.org/10.1016/0273-1177\(92\)90040-5](https://doi.org/10.1016/0273-1177(92)90040-5)
- Ridley, A. J., Deng, Y., & Tóth, G. (2006). The global ionosphere-thermosphere model. *Journal of Atmospheric and Solar-Terrestrial Physics*, 68(8), 839–864. <https://doi.org/10.1016/j.jastp.2006.01.008>
- Roble, R. G., & Ridley, E. C. (1994). A thermosphere-ionosphere-mesosphere-electrodynamics general circulation model (time-GCM): Equinox solar cycle minimum simulations (30–500 km). *Geophysical Research Letters*, 21(6), 417–420. <https://doi.org/10.1029/93gl03391>
- Ruohoniemi, J. M., & Greenwald, R. A. (1996). Statistical patterns of high-latitude convection obtained from Goose Bay HF radar observations. *Journal of Geophysical Research*, 101(A10), 21743–21763. <https://doi.org/10.1029/96ja01584>
- Schlegel, K., Lühr, H., St.-Maurice, J.-P., Crowley, G., & Hackert, C. (2005). Thermospheric density structures over the polar regions observed with CHAMP. *Annals of Geophysics*, 23(5), 1659–1672. <https://doi.org/10.5194/angeo-23-1659-2005>
- Shepherd, S. G. (2014). Altitude-adjusted corrected geomagnetic coordinates: Definition and functional approximations. *Journal of Geophysical Research: Space Physics*, 119(9), 7501–7521. <https://doi.org/10.1002/2014ja020264>
- Sutton, E. K., Forbes, J. M., & Knipp, D. J. (2009). Rapid response of the thermosphere to variations in Joule heating. *Journal of Geophysical Research: Space Physics*, 114(A4). <https://doi.org/10.1029/2008ja013667>
- Thayer, J. P., Vickrey, J. F., Heelis, R. A., & Gary, J. B. (1995). Interpretation and modeling of the high-latitude electromagnetic energy flux. *Journal of Geophysical Research*, 100(A10), 19715–19728. <https://doi.org/10.1029/95ja01159>
- Thébault, E., Finlay, C. C., Beggan, C. D., Alken, P., Aubert, J., Barrois, O., et al. (2015). International geomagnetic reference field: The 12th generation. *Earth, Planets and Space*, 67(1), 79. <https://doi.org/10.1186/s40623-015-0313-0>
- Thomas, E. G., & Shepherd, S. G. (2018). Statistical patterns of ionospheric convection derived from mid-latitude, high-latitude, and polar SuperDARN HF radar observations. *Journal of Geophysical Research: Space Physics*, 123(4), 3196–3216. <https://doi.org/10.1002/2018ja025280>
- Walterscheid, R. L. (1989). Solar cycle effects on the upper atmosphere - Implications for satellite drag. *Journal of Spacecraft and Rockets*, 26(6), 439–444. <https://doi.org/10.2514/3.26089>

- Wang, X., Miao, J., Aa, E., Ren, T., Wang, Y., Liu, J., & Liu, S. (2020). Statistical analysis of Joule heating and thermosphere response during geomagnetic storms of different magnitudes. *Journal of Geophysical Research: Space Physics*, *125*(8), e2020JA027966. <https://doi.org/10.1029/2020ja027966>
- Waters, C. L., Anderson, B. J., Greenwald, R. A., Barnes, R. J., & Ruohoniemi, J. M. (2004). High-latitude poynting flux from combined Iridium and SuperDARN data.
- Weimer, D. R. (2005). Improved ionospheric electrodynamic models and application to calculating Joule heating rates. *Journal of Geophysical Research: Space Physics*, *110*(A5). <https://doi.org/10.1029/2004ja010884>
- Wilson, G. R., Weimer, D. R., Wise, J. O., & Marcos, F. A. (2006). Response of the thermosphere to Joule heating and particle precipitation. *Journal of Geophysical Research: Space Physics*, *111*(A10). <https://doi.org/10.1029/2005ja011274>
- Yamazaki, Y., Kosch, M. J., & Sutton, E. K. (2015a). A model of high-latitude thermospheric density. *Journal of Geophysical Research: Space Physics*, *120*(9), 7903–7917. <https://doi.org/10.1002/2015ja021371>
- Yamazaki, Y., Kosch, M. J., & Sutton, E. K. (2015b). North-south asymmetry of the high-latitude thermospheric density: IMF B Y effect. *Geophysical Research Letters*, *42*(2), 225–232. <https://doi.org/10.1002/2014gl062748>
- Yeoman, T. K., Chisham, G., Baddeley, L. J., Dhillon, R. S., Karhunen, T. J. T., Robinson, T. R., et al. (2008). Mapping ionospheric backscatter measured by the SuperDARN HF radars - Part 2: Assessing SuperDARN virtual height models. *Annals of Geophysics*, *26*, 843–852. <https://doi.org/10.5194/angeo-26-843-2008>
- Zhang, X. X., Wang, C., Chen, T., Wang, Y. L., Tan, A., Wu, T. S., et al. (2005). Global patterns of Joule heating in the high-latitude ionosphere. *Journal of Geophysical Research: Space Physics*, *110*(A12). <https://doi.org/10.1029/2005ja011222>